

Maximum Likelihood Estimation of Shear Wave Speed in Transient Elastography

Stéphane Audière*, *Member, IEEE*, Elsa D. Angelini, *Senior Member, IEEE*, Laurent Sandrin, and Maurice Charbit

Abstract—Ultrasonic transient elastography (TE), enables to assess, under active mechanical constraints, the elasticity of the liver, which correlates with hepatic fibrosis stages. This technique is routinely used in clinical practice to assess noninvasively liver stiffness. The Fibroscan system used in this work generates a shear wave via an impulse stress applied on the surface of the skin and records a temporal series of radio-frequency (RF) lines using a single-element ultrasound probe. A shear wave propagation map (SWPM) is generated as a 2-D map of the displacements along depth and time, derived from the correlations of the sequential 1-D RF lines, assuming that the direction of propagation (DOP) of the shear wave coincides with the ultrasound beam axis (UBA). Under the assumption of pure elastic tissue, elasticity is proportional to the shear wave speed. This paper introduces a novel approach to the processing of the SWPM, deriving the maximum likelihood estimate of the shear wave speed when comparing the observed displacements and the estimates provided by the Green's functions. A simple parametric model is used to interface Green's theoretical values of noisy measures provided by the SWPM, taking into account depth-varying attenuation and time-delay. The proposed method was evaluated on numerical simulations using a finite element method simulator and on physical phantoms. Evaluation on this test database reported very high agreements of shear wave speed measures when DOP and UBA coincide.

Index Terms—Elasticity, Green's function, likelihood function, liver, shear wave, transient elastography, ultrasound.

I. INTRODUCTION

OVER the last two decades, several shear-wave based elastography approaches have been investigated to measure the mechanical properties of biological soft tissues [1]–[7]. A review of ultrasound elastography techniques can be found in [8] that includes short descriptions of the different techniques of acquisition currently available along with recommendations on their clinical use. Elastography is particularly useful to assist the diagnosis of liver fibrosis based on the assumption that the stage of fibrosis is directly related to the measured elasticity [9], [10].

Manuscript received January 30, 2014; accepted March 04, 2014. Date of publication March 12, 2014; date of current version May 29, 2014. *Asterisk indicates corresponding author.*

*S. Audière is with Echosens, 75013 Paris, France (e-mail: stephane.audiere@echosens.com).

E. D. Angelini is with the Institut Mines-Telecom, Telecom ParisTech, CNRS LTCI, 75013 Paris, France, and also with the Department of Biomedical Engineering, Heffner Biomedical Imaging Laboratory, Columbia University, New York, NY 10027 USA (e-mail: elsa.angelini@telecom-paristech.fr).

L. Sandrin is with Echosens, 75013 Paris, France (e-mail: laurent.sandrin@echosens.com).

M. Charbit is with the Institut Mines-Telecom, Telecom ParisTech, CNRS LTCI, 75013 Paris, France (e-mail: maurice.charbit@telecom-paristech.fr).

Digital Object Identifier 10.1109/TMI.2014.2311374

Elasticity is defined by the Young's modulus E and is related, under linear elastic assumptions, to the shear wave speed V_s inside the liver through the relation $E = 3\rho V_s^2$ where ρ denotes the mass density of the tissue [11]. Since most biological tissues are essentially composed of water, ρ may be taken equal to 1000 kg/m^3 .

In transient elastography (TE), a mild excitation is caused by a piston which produces two elastic waves in the tissue: a compression wave and a shear wave. The compression wave travels too fast to be tracked with ultrasound, while the shear speed is slow enough to be deduced from the RF line recordings. A general review on transient elastography applied to the detection of hepatic fibrosis can be found in [12]. The Fibroscan (Echosens, Paris, France) system used in this work is based on this technique [1]. The piston is excited with a short pulse, typically designed as a single period of a sine wave, whose frequency ranges between 50 and 1000 Hz. This short pulse induces a stress constraint at the surface of the tissue. The shear wave speed V_s is estimated through the evaluation of displacements of RF lines within the liver. A common way to access the displacement field is to use ultrasonic scanning and measure correlations between successive RF lines observed along a fixed ultrasound beam axis (UBA) using a single element ultrasonic probe. The resultant parametric image is called a shear wave propagation map (SWPM). Such approach usually assumes that the UBA coincides with the direction of propagation (DOP) of the shear-wave.

Two categories of methods are used to calculate the shear wave speed from RF lines recorded within a homogeneous medium, based on the inversion of the shear wave propagation equation or based on the calculation of the time of flight (TOF). The first strategy is often applied in magnetic resonance elastography (MRE) [13][14] but is not suited for ultrasound elastography. Indeed, this method relies either on second order derivatives which are particularly delicate to estimate in the case of low signal to noise ratio as can be encountered in ultrasound or on the knowledge of 3-D displacements components which are not available with TE. TOF techniques are most commonly employed in ultrasound elastography as in acoustic radiation force impulse (ARFI) [5] where an ultrasound radiation force is generated in tissues using a conventional ultrasound probe, and a TOF algorithm (e.g., Lateral Time to Peak algorithm in [15]) is used to calculate the shear wave speed from the tracked displacements. Supersonic shear imaging (SSI) [4] and the Fibroscan also use a TOF algorithm to estimate the shear wave speed by computing the slope of the peak displacement values observed on the SWPM. The TOF approach is model-free and does not take into account the physics of propagation such as

the diffraction patterns and the coupling between the shear and compression waves that can lead to complex SWPM patterns.

Numerical simulations using finite element models (FEM) are popular tools to study the interactions between a traveling wave and the medium of propagation. In the context of elastography acquisitions, numerical simulations were used by Palmeri *et al.* [16] to study the propagation of waves induced by the ARFI method, by Chen *et al.* [17] to study the shear waves induced by MRE on a simple geometrical model and by Bastard *et al.* [18] to solve the wave equation applied in transient elastography via a pseudo-spectral finite difference method. These numerical simulations provide extremely rich insights on the behavior of a given elastography setup but remain limited regarding the number of degrees of freedom that can be used to model the environment (i.e., geometry of the interface, characteristics of the stress source, heterogeneities within the medium, etc.) while preserving reasonable computation times.

II. METHOD

A. Transient Elastography System Setup and Computations

TE Setup: The TE system being studied uses a circular piston that impacts the surface of a homogeneous object (regarded as a semi-infinite medium), and induces, in addition to a pressure wave, a shear wave that propagates longitudinally along its DOP. The frequency and wavelength of the shear wave, denoted f_s and λ_s , depend on the stress constraint applied on the piston. In this work, we denote by $a(t)$ this stress constraint, and model it as a sinusoid with frequency f_a . When used *in vivo*, this setup assumes that the dimension of the screened organ is larger than λ_s . In the liver, the elasticity E is in the range [1–75] kPa [1], corresponding to a shear-wave speed V_s in the range [0.6–5] m/s. Hence, using the relation $V_s = \lambda_s f_s$ and assuming, as a rough approximation, that $f_s = f_a$ for the TE setup, if we apply constraints with frequencies f_a of {50, 100, 150} Hz, the wavelength λ_s falls in the ranges {[1.2–10], [0.6–5], [0.4–3.3]} cm. The dimension of an average adult liver being (28 × 16 × 8) cm, the shear wave wavelength therefore remains smaller than the long dimension of the liver, which is aligned with the UBA.

Generation of SWPMs: The TE system measures along the UBA the displacements of the points within the medium, via classical spatio-temporal correlation of RF lines, composing what we call the shear-wave parametric map (SWPM), illustrated in Fig. 3. This TE setup assumes that the UBA is aligned with the DOP and corresponds to the configuration used in [19]. We have shown in [20] that this TE setup can be simulated numerically with high accuracy for detailed analysis of the shear wave propagation phenomena and replication of SWPM artefacts such as rebounds.

Estimates of V_s on SWPM: To estimate the shear wave speed V_s , the standard time of flight (TOF) approach computes the slope of the peak displacements on the SWPM. Unfortunately, this approach is not robust to physical artefacts that can be observed on SWPMs such as rebounds or to physics effects such as diffraction and coupling of the pressure and the shear waves [19].

Proposed Computational Pipeline With ML Estimators: In this work, we propose a new computational pipeline to derive

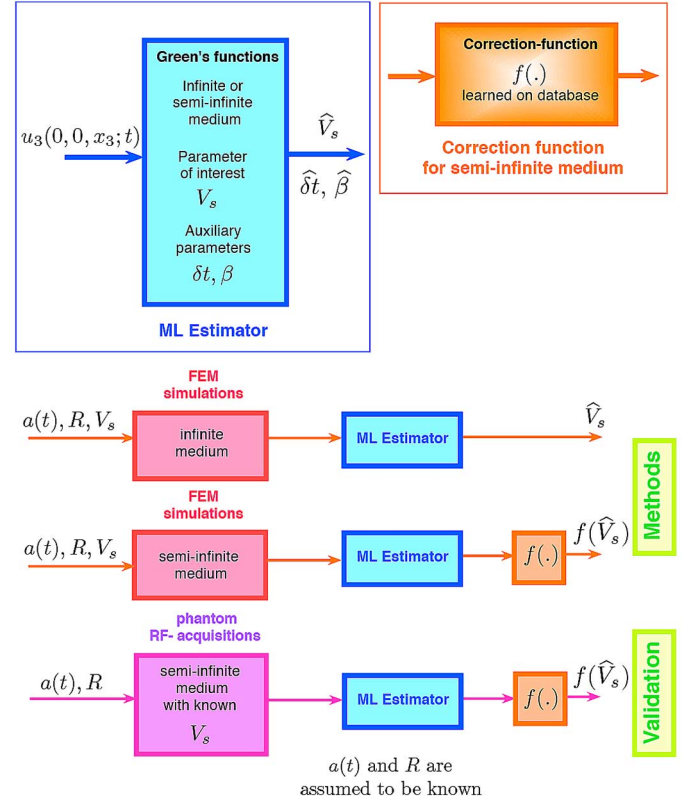


Fig. 1. Computational and validation pipelines of the proposed ML estimator of the shear wave speed \hat{V}_s inside a homogeneous medium based on Green's functions, FEM simulations and RF TE recordings on phantom objects. Input of the ML estimator are the properties of the hitting cylindrical piston (radius R and displacement profile $a(t)$) and the resulting displacements u_3 induced by the shear wave inside the medium. Distinct processing pipelines are proposed depending on the geometry of the medium: infinite (purely theoretical configuration) or semi-infinite (experimental configuration).

V_s from the SWPM measures, which was partially introduced in [21] and is outlined in Fig. 1. The input variables, encoding the TE setup are the sinusoidal stress constraint $a(t)$ (with frequency f_a) that controls the cylindrical piston, and the radius R of the piston. The piston is assumed to act normally on the planar medium interface. The measures recorded by the TE system are the longitudinal displacement components u_3 (along the UBA) of the displacement vectors $u = [u_1 \ u_2 \ u_3]$ generated by the shear wave propagating in the medium. These measures are recorded in the SWPM which displays u_3 as a function of depth (along the UBA axis denoted x_3) and time t . The output of the computational pipeline is the ML estimate (either \hat{V}_s or $f(\hat{V}_s)$ in Fig. 1) of the shear wave speed V_s , which characterizes the elasticity of the medium.

The proposed computational pipeline exploits an original maximum likelihood (ML) criterion (blue box in Fig. 1), modeling the SWPM measures as noisy random variables. Computation of the ML estimate \hat{V}_s requires two steps: first, analytical displacement values are computed using the Green's functions; then, a ML criterion is maximized to optimize the match between the measured and the analytical displacement values. The proposed approach takes advantage of our knowledge of the analytical expression of the Green's functions that were derived by Sandrin *et al.* [19] for the TE setup being

studied. These Green's functions provide an explicit relationship between the stress $a(t)$ applied by the circular piston on the medium and the displacement field u_3 observed within this medium, under some specific boundary conditions that must be specified on the limits of the medium. As will be discussed later on, the Green's functions derived in [19] are exact for an infinite medium but not for a semi-infinite medium. For this reason we propose to exploit numerical simulations (cf. next paragraph and the pink boxes in Fig. 1) to learn three correction factors required in the computational pipeline: auxiliary variables δt and β in the ML estimator and a correction function f for \hat{V}_s (orange box in Fig. 1).

FEM Simulations as a Numerical Laboratory: A FEM simulation tool was used as a numerical laboratory to design the proposed computational pipeline. In particular, it was used to test the adequacy and robustness of the analytical displacement values derived from the Green's functions. A large amount of synthetic observations was generated by propagating a shear wave in an infinite or semi-infinite medium, corresponding respectively to a purely theoretical and an experimental configuration such as within a cylindrical phantom. This rich set of synthetic data was used for the following tasks. 1) It led us to introduce two auxiliary variables in the ML estimator (blue box in Fig. 1): a multiplicative depth-varying attenuation factor $\beta(x_3)$ and a time delay δt . Both variables are configuration-dependent and must be estimated along with \hat{V}_s when optimizing the ML criterion. 2) It enabled us to test and document the variability of these auxiliary variables with respect to the experimental configurations (e.g., infinite versus finite medium). 3) It served as our ground truth to validate the formulation of the ML criterion. 4) It revealed that in a semi-infinite medium, an additional adjustment needed to be made to correctly estimate V_s from \hat{V}_s . A correction function, denoted $f(\cdot)$ (orange box in Fig. 1) was therefore introduced in the pipeline and learned on a database of simulated SWPMs.

Validation: The accuracy of the proposed ML estimator was evaluated on RF lines acquired on three homogeneous phantom objects with known physical properties and one heterogeneous phantom containing spherical objects of different elasticity.

To summarize, we derive in this section a ML estimator to infer the shear wave speed V_s from displacements observed inside a medium with an ultrasonic TE system. The proposed ML estimator requires some modeling of the displacement measures, viewed as corrupted observations of the true displacements $u_3(0, 0, x_3, t)$ and the use of analytical predictions of the displacement values computed with simplified Green's functions previously derived for the corresponding experimental conditions. We now detail each component of this computational pipeline.

B. Analytical Predictions of Displacements From the Green's Functions

To introduce the Green's functions, we model the medium as elastic and infinite, and associate a Cartesian coordinate system (x_1, x_2, x_3) . The medium contains no body force and a traction (stress) T , expressed in Pascal (N/m²) is applied on the plane

$x_3 = 0$, along the direction $x_3 \geq 0$, by a circular piston of radius R and circular section $\mathcal{C}(R)$ centered at the origin of the coordinate system. It follows (see [22, (5)]) that the displacement field created within the medium at the position $\underline{x} = [x_1 \ x_2 \ x_3]^T$ and at the time t writes

$$u_n(\underline{x}, t) = \int_{-\infty}^{+\infty} d\tau \left(\int_{\mathcal{C}(R)} \int_{\mathcal{C}(R)} T_i(\underline{\xi}, \tau) G_{in}(\underline{\xi}, t - \tau; \underline{x}, 0) d\xi_1 d\xi_2 - \int_{\mathbb{R}^2} u_i(\underline{\xi}, \tau) c_{i3kl}(\underline{\xi}) G_{kn,l}(\underline{\xi}, t - \tau; \underline{x}, 0) d\xi_1 d\xi_2 \right) \quad (1)$$

where $\underline{\xi} = [\xi_1 \ \xi_2 \ 0]^T$, $i, j, k, l, n \in \{1, 2, 3\}$ are indexes which refer to the coordinate system, $c_{ijkl}(\underline{\xi})$ is the $ijkl$ -entry of the elastic modulus tensor, $T_i(\underline{x}, t)$ is the i th component of T , $G_{in}(\underline{\xi}, \tau; \underline{x}, t)$ is the dyadic elastodynamic Green's function, and $G_{kn,l} = \partial G_{kn}(\underline{\xi}, \tau; \underline{x}, t) / \partial x_l$. Summations on i, k, l are assumed in (1).

For a homogeneous, isotropic and infinite solid, elastic propagation is governed by the fundamental equation of Navier. In this case, the dyadic Green's functions have been developed successively by Love in 1944 [23], Achenbach in 1973 [24] and Aki and Richard in 1980 [25]. They are recalled in [22, (2)]. These Green's functions G_{ij} are the sum of three terms: a term associated with the compression wave, a term associated with the shear wave and a third one being a coupling term. In soft medium, as in the liver, the speed of propagation of the compression wave ($V_c = 1500$ m/s) is approximately 1000 times higher than the speed of propagation of the shear wave. The compression wave speed is therefore too fast to be measurable by an ultrasound probe, leading to the commonly-used approximation in ultrasonic elastography that sets to zero the compression term while preserving the shear and coupling terms. As an alternative the curl-operator has been proposed in [26] to separate the components induced by the compression and the shear waves on displacement fields recorded with MRE. For TE setups, the use of dyadic Green's functions to infer and decompose the generated displacement fields while assuming a zero compression term was derived theoretically for an infinite medium, and later extended to a semi-infinite medium in [22].

In the following, we consider that the traction is uniformly distributed on the circular section $\mathcal{C}(R)$ of the piston located in the plane $x_3 = 0$ and is given by

$$\begin{cases} T_1 = T_2 = 0 \\ T_3(x_1, x_2, x_3, t) = \mathbb{1}((x_1, x_2, x_3) \in \mathcal{C}(R)) a(t) \end{cases} \quad (2)$$

where $\mathbb{1}(\cdot)$ is the indicator function, and $a(t)$ a time dependent traction expressed in Pascal.

Unfortunately, the integral formula in (1) gives only an implicit expression of the displacements u_n as the u_i components appear in the right hand side. Therefore, computation of the integral requires complex numerical schemes. In [22] the authors proposed to neglect the implicit terms in the integral, by assuming that the traction only generates bulk waves and no

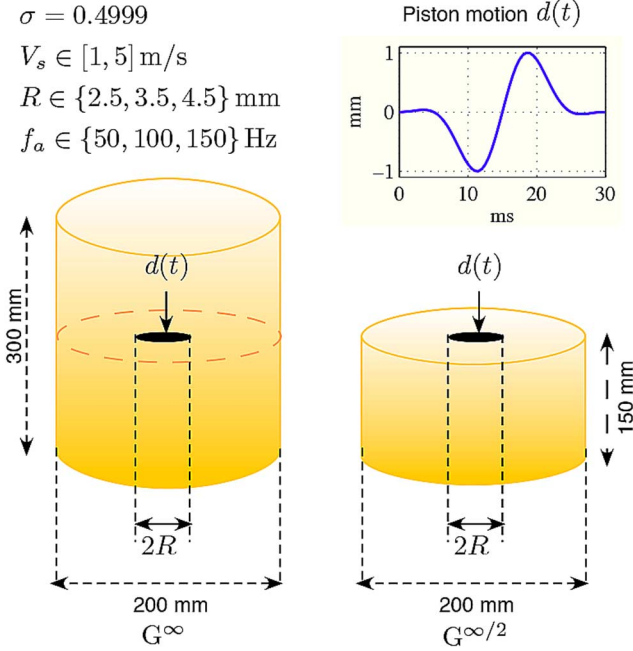


Fig. 2. FEM axis-symmetric geometries. G^∞ : piston positioned at the center of the medium. $G^{\infty/2}$: piston positioned at the surface of the medium.

surface wave. Based on this approximation, the mathematical expression of the displacements induced in a semi-infinite medium, along the DOP, after stimulation at its interface by an impulse applied with a circular piston of radius R , was derived by Sandrin *et al.* [19], matching the experimental conditions used by the TE system. The closed form expression writes

$$\begin{cases} u_1(0, 0, x_3, t) = u_2(0, 0, x_3, t) = 0 \\ u_3(0, 0, x_3, t) = \frac{R^2}{\rho} \frac{1}{(x_3^2 + R^2)^{3/2}} \int_0^{\tau_s} \tau a(t - \tau) d\tau \end{cases} \quad (3)$$

where the integral upper-limit is given by

$$\tau_s = \frac{\sqrt{R^2 + x_3^2}}{V_s}. \quad (4)$$

For a purely elastic medium (analogous to a spring), the relation between the displacement $d(t)$ of the piston and the stress $a(t)$ induced in the medium is linear, enabling to generate accurate numerical simulations when modeling the constraint as a displacement of the piston (cf. Fig. 2). We notice that the expression in (3) only allows to compute the induced displacement field $u_3(\cdot; t)$ for points along the x_3 axis. For points within the medium but away from the x_3 axis, no analytical closed form expressions are known but numerical integrations are always possible, at a much higher computational cost.

C. FEM Simulation of the Shear Wave Propagation

Following our preliminary work in [20] we propose to use a FEM simulation tool (COMSOL Multiphysics, COMSOL, Stockholm, Sweden), capable of propagating a mechanical wave in a homogeneous or heterogeneous and elastic or visco-elastic medium. To design our computational pipeline, transient elastography experiments are simulated for a purely elastic medium and a simple geometry using an axisymmetric

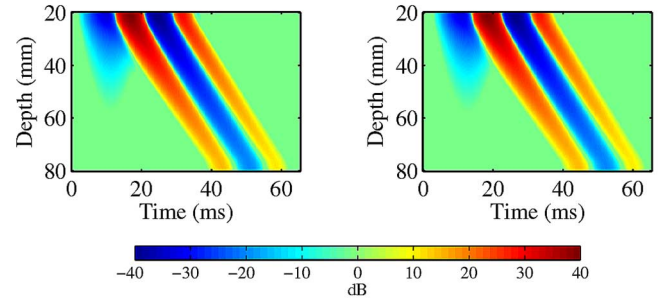


Fig. 3. Comparison of SWPMs for the $G^{\infty/2}$ geometry, $V_s = 2 \text{ m/s}$, $f_a = 50 \text{ Hz}$, and $R = 4.5 \text{ cm}$. (left) SWPM of FEM-based $u_3^F(0, 0, x_3; t)$. (right) SWPM of Green's-based $u_3^G(0, 0, x_3; t)$.

cylinder. Since the analytical displacements formulated in (3) for a semi infinite medium screened with the TE system were initially derived for an infinite medium, we study two different geometries, as illustrated in Fig. 2.

G^∞ : the constraint is applied inside the medium, with the stress source positioned in the middle of the longitudinal axis of the cylinder. The cylinder dimensions are set to: 300 mm high and 200 mm wide. It does not represent a realistic experimental set up but enables to simulate an infinite medium by preventing rebounds of the wave at the surfaces of the cylinder and creation of surface waves over the short simulation time.

$G^{\infty/2}$: the piston hits the cylinder object on its upper surface. The cylinder dimensions were set to: 150 mm high and 200 mm wide.

For both geometries, the origin of the x_3 axis is placed at the position of the stress source, and we only illustrate SWPMs for $x_3 \geq 0$ for the G^∞ geometry.

1) *Parameterization of the Simulations*: Numerical simulations focus on replicating scanning situations encountered with the use of the Fibrosan TE system for liver screening. We therefore work with the following ranges of values for the simulation parameters.

- Geometry: G^∞ or $G^{\infty/2}$.
- Condition on the borders of the domain: free deformations.
- Pulse frequency: $f_a \in \{50, 100, 150\} \text{ Hz}$, (usable frequencies with the Fibrosan TE probes in research mode).
- Piston radius: $R \in \{2.5, 3.5, 4.5\} \text{ mm}$, (corresponding to existing Fibrosan TE probes).
- Medium characteristics: $V_s \in [1, 5] \text{ m/s}$ by increment of 0.1 m/s, corresponding to elasticity values from 3 to 75 kPa as encountered in the liver, and a Poisson ratio $\sigma = 0.4999$, which corresponds to an incompressible medium.

Using all possible combinations of these parameters leads to a total of 369 simulations per geometry. In all simulations, the UBA is assumed to coincide with the DOP and the piston motion $d(t)$ is defined as a single period sinusoid apodized with a Gaussian kernel. The maximum size of the finite element triangular mesh is set to $\lambda_s/20$, where λ_s represents the shear wave wavelength. This mesh size is required to guarantee numerical stability of the solver. Such parameterization is consistent with the work of Roth *et al.* [27]. Finally, the tolerance level used to assess convergence is set to $0.01 \mu\text{m}$. The COMSOL FEM software tool does not allow to use absorbing borders [also called

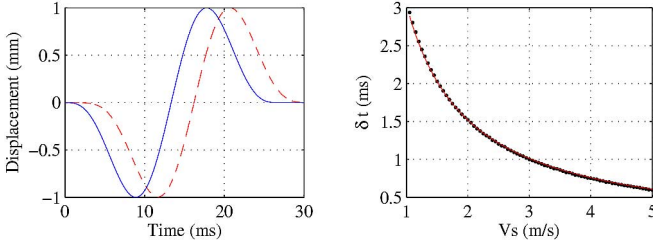


Fig. 4. Left side: Comparison of displacements from $u_3^F(0, 0, 0, t)$ (solid line) and $u_3^G(0, 0, 0, t)$ (dashed line) with parameters: G^∞ geometry, $f_a = 50$ Hz and $R = 4.5$ cm. Right side: time shift δt at depth 0 mm versus shear wave speed V_s for the same stimulation configuration. Markers (\bullet) correspond to measured values and the solid line represents the fit $3.04/V_s$.

perfect match layer (PML)] when running temporal simulations. Therefore we have to rely on the use of a domain large enough to avoid rebounds in the time window of the observations. Using the cylinder dimensions reported in Fig. 2, we confirm in Fig. 3 that for $V_s = 2$ m/s we do not see any rebound. On the other hand, in Fig. 6, when $V_s = 5$ m/s (highest value), some rebounds are visible but do not interfere with the signal of interest.

For a given set of parameters R , f_a , V_s , and G^∞ or $G^{\infty/2}$ geometry we generate:

- $u_3^F(x_1, x_2, x_3; t)$ which denotes the displacement values at the output of the FEM simulation;
- $u_3^G(x_1, x_2, x_3; t)$ which denotes the analytical displacement values from (3) derived from Green's analysis.

2) *Comparison of FEM and Green's Displacements*: The SWPMs of the displacements $u_3^F(0, 0, x_3; t)$ and $u_3^G(0, 0, x_3; t)$ are reported in Fig. 3 as a function of time (between 0 and 60 ms) and depth (between 20 and 80 mm) for the following parameters: $G^{\infty/2}$ geometry, $R = 4.5$ mm, $f_a = 50$ Hz, and $V_s = 2$ m/s. The amplitude is encoded in color using a logarithmic scale. On both images, the blue area at the onset of the displacements corresponds to the coupling effect between the shear and compression waves.

Visually, the two SWPMs seem to match perfectly, but numerical comparison of individual profiles along time at a given depth, as illustrated in Fig. 4 at depth 0 mm, reveal a systematic offset δt of the temporal onsets of the displacements u_3^G when compared to u_3^F . The response from the solver is systematically ahead in time when compared to the response provided by the Green's analytical functions, using either the $G^{\infty/2}$ or G^∞ geometries.

In our series of simulations, we observed that, for a given set of values (R, f_a, G) , the time shift δt varies with V_s but remains almost constant as a function of depth. As an illustration, we plot on the left curves of the Fig. 4 the displacements $u_3^F(0, 0, 0, t)$ and $u_3^G(0, 0, 0, t)$ for simulations with the G^∞ geometry, $f_a = 50$ Hz and $R = 4.5$ mm. We can see that the "true" displacement values $u_3^F(0, 0, 0, t)$ are in advance with respect to the analytical values $u_3^G(0, 0, 0, t)$ derived from the Green's analysis, by a time shift δt . As seen on the right displays of Fig. 4, the observed values of this time shift can be accurately fitted by the regression function $3.04/V_s$ where V_s is expressed in m/s and δt in ms. We observed that the time shift also varies with R , f_a and G . Overall, the series of simulations showed that no simple parametric model between all these parameters can be

learned to efficiently predict the value of δt , given a particular set of configuration values (R, f_a, G) and V_s . We therefore include δt as an auxiliary variable in the expression of u_3 to be used in the ML criterion, and estimate its value along with V_s .

D. Maximum Likelihood Estimator of V_s

1) *Formulation*: We can record, with the TE system or via simulations, observations $y[m, n]$ of the displacements inside a medium under the considered TE experimentation protocol, sampled in space along the UBA x_3 and in time t . These observed displacements can be compared to their corresponding Green's analytical predictions provided by (3). To set up such comparison, we model the discrepancy between the observed displacements $y[m, n]$ and the model given by (3) as a Gaussian random sequence. We include in the model the following components that were found sufficient to explain the discrepancies.

- A depth-dependent multiplicative attenuation factor $\beta[m]$. This factor takes into account the unknown depth-dependent and medium-dependent attenuation of the RF signals acquired by the TE system.
- An additive Gaussian random noise term $w[m, n]$ with zero-mean and a constant unknown variance. This term takes into account the measurement noise.
- A time shift δt known to exist between the simplified Green's functions used in this work and the real displacements (cf. Section II-C2).

We then write

$$y[m, n] = \beta[m]u_3[m, n; V_s; \delta t] + w[m, n] \quad (5)$$

where, for a medium with shear wave speed V_s and for a given δt , $u_3[m, n; V_s; \delta t] = u_3(0, 0, mZ_s; nT_s + \delta t)$, using (3). T_s and Z_s denote respectively the time period and the depth period and indexes n and m go respectively from 1 to N and from 1 to M .

We denote by $\mu = (\beta, V_s, \delta t)$ the parameters of interest to estimate from the observations y , using the model in (5). Under Gaussian assumption, the maximum likelihood (ML) approach leads to a ML estimate $\hat{\mu}$ that minimizes the following criterion:

$$\hat{\mu} = \underset{\mu}{\operatorname{argmin}} \sum_{m=1}^M \sum_{n=1}^N (y[m, n] - \beta[m]u_3[m, n; V_s; \delta t])^2. \quad (6)$$

Minimization with respect to β is performed by canceling analytically its partial derivative. Minimization with respect to V_s and δt yields to the following ML criterion (see Appendix for computational details)

$$G(V_s, \delta t) = \sum_{m=1}^M \frac{\left(\sum_{n=1}^N y[m, n]u_3[m, n; V_s; \delta t] \right)^2}{\sum_{n=1}^N u_3^2[m, n; V_s; \delta t]} \quad (7)$$

$$(\hat{V}_s, \hat{\delta t}) = \underset{(V_s, \delta t)}{\operatorname{argmax}} G(V_s, \delta t).$$

The ML estimates $(\hat{V}_s, \hat{\delta t})$ correspond to the position where the function $G(V_s, \delta t)$ reaches its global maximum.

2) *Implementation*: No analytical expression can be derived for the maximization of the ML criterion in (7) and we therefore

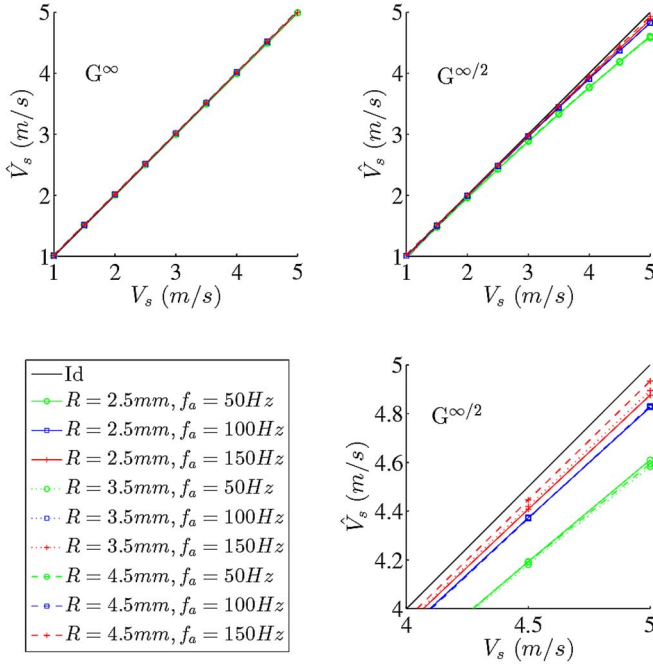


Fig. 5. Relation between \hat{V}_s and V_s using FEM simulations on two geometries: (left) G^∞ , (right) $G^{\infty/2}$, and nine constraint setups with varying values of R = piston radius and f_a = central frequency of the piston constraint $a(t)$. The lower right plot is a zoom from for the upper right plot.

rely on an exhaustive search on a fine grid of values $(V_s, \delta t)$. To optimize computation time, an initial search can be performed on a coarse grid of values, further refined on a finer grid around the values returning the maximum of the ML criterion on the coarse grid.

For a heterogeneous medium (e.g., a phantom with hard/soft inclusions), the ML estimations must be performed within localized spatial windows, which size and overlap must be set to optimize the tradeoff between computation time and spatial resolution of the shear wave speed estimation. Such implementation of the ML estimator will be illustrated in Section III.

E. Regression Adjustment of \hat{V}_s for Semi-Infinite Mediums

The use of auxiliary variables and the proposed ML criterion lead to perfect agreements between the corrected Green's analytical predictions and the FEM-simulated displacement values in an infinite medium, as illustrated in Fig. 5, but not in a semi-infinite one. Indeed, the simplified analytical expression of the Green's functions for a semi-infinite medium was derived by multiplying by a factor two the Green's functions defined for an infinite medium. This solution, proposed in [22], assumes baffled conditions for the transducer [28], [29], and is based on the so-called image method [30] (or method of mirror images) which is a mathematical tool used to solve differential equations, in which the domain of the sought function is extended by the addition of its mirror image with respect to a symmetry hyperplane. With such a simple model, surface phenomena are not taken into account by the $G^{\infty/2}$ geometry Green's functions, while surface and compression waves influence the shear wave propagation, which is correctly reproduced by the FEM simulations.

We propose to learn on FEM simulations generated in semi-infinite mediums the relation between \hat{V}_s and the ground-truth value V_s via the definition of a polynomial function f so that: $V_s = f(\hat{V}_s)$.

1) *FEM-Based Comparison of \hat{V}_s Versus V_s* : Our comparison pipeline, illustrated in Fig. 6, uses the following computational steps.

- 1) FEM simulation of displacements u_3^F using V_s .
- 2) ML estimation of \hat{V}_s on u_3^F .
- 3) Inference of the correction function $f(\hat{V}_s)$.
- 4) Green's simulations of displacements u_3^G using $f(\hat{V}_s)$ and δt .

Out of this pipeline, we compare the following values: \hat{V}_s versus V_s versus $f(\hat{V}_s)$ and u_3^F versus u_3^G using $f(\hat{V}_s)$.

In the example illustrated in Fig. 6, the FEM simulator is used using the $G^{\infty/2}$ geometry, $V_s = 5$ m/s, $R = 4.5$ mm, and $f_a = 50$ Hz. On the top left the FEM-simulated SWPM is displayed, encoding the amplitude of the axial displacements u_3^F in colors, as a function of time in ms and depth in mm. On the top right, the parametric map of the ML criterion from (7) with respect to the pair of parameters $(V_s, \delta t)$ is displayed. It is evaluated on a grid of $(V_s, \delta t)$ values in the range $[0-5.5]$ m/s for V_s and $[-5 - 5]$ ms for δt and using steps of $(0.1 \text{ m/s}, (2)/(PRF))$ s for the coarse estimations and $(0.01 \text{ m/s}, (1)/(PRF))$ s for the refined estimations, where PRF is the pulse repetition frequency (in Hertz) used by the TE system. In the illustrated experiment, the maximum of the ML criterion was reached at $\hat{V}_s = 4.53$ m/s.

Plots of \hat{V}_s versus V_s for the series of 369 simulations generated with nine different configurations (cf. Section II-C1) are provided in Fig. 5 and confirm that the MLE provides perfect estimates of V_s with the proposed measurement model in an infinite medium (correlation measures R^2 above 0.99 and relative errors below 1%). In a semi-infinite medium, there are discrepancies between \hat{V}_s and V_s which vary with the tested configuration and increase with V_s . The zoom in Fig. 5, suggests that a quadratic correction of \hat{V}_s might suffice but requires different coefficients for different constraint configurations. The proposed correction function for a semi-infinite medium is written as

$$f(\hat{V}_s) = c_2(R, f_a)\hat{V}_s^2 + c_1(R, f_a)\hat{V}_s + c_0(R, f_a). \quad (8)$$

We learn the (c_2, c_1, c_0) coefficients for each of the configurations simulated with the $G^{\infty/2}$ geometry by minimizing the root mean square error over all V_s values. The coefficients learned on six of the nine configurations tested in Fig. 5, using only radius values R available on the commercialized Fibroscan TE probes, are reported in Table I. Using the correction function, we obtained a coefficient of correlation R^2 between V_s and $f(\hat{V}_s)$ superior to 0.99 and relative errors that remained below 10%. In the example of Fig. 6, the corrected value of the estimated shear wave speed ended up to be $f(\hat{V}_s) = 4.91$ m/s. On the bottom left of this figure we illustrate the analytical SWPM of u_3^G using $f(\hat{V}_s)$ and δt .

To conclude this part, we therefore propose to adjust the ML estimates \hat{V}_s as follows: no correction for the G^∞ geometry, a quadratic correction for the $G^{\infty/2}$ geometry with coefficients

TABLE I
COEFFICIENTS OF THE CORRECTION FUNCTION IN (8) LEARNED FOR SIX CONFIGURATIONS (R, f_a) VIA FEM SIMULATIONS ON A SEMI-INFINITE MEDIUM

f_a (Hz)	$R = 2.5$ mm			$R = 4.5$ mm		
	c_2	c_1	c_0	c_2	c_1	c_0
50	0.026	0.959	0.026	0.037	0.896	0.096
100	0.018	0.934	0.076	0.011	0.980	0.001
150	0.012	0.955	0.056	0	1.026	-0.054

TABLE II
AVERAGE MEASURES (\pm STANDARD DEVIATION) OF V_s ESTIMATES ON THE HOMOGENEOUS PHANTOMS AS PROVIDED BY CIRS (V_s CIRS) AND ESTIMATED AT TWO DEPTH RANGES WITH THE FIBROSCAN TE SYSTEM USING TOF (V_s TOF) AND THE PROPOSED ML ESTIMATION METHOD ($f(\hat{V}_s)$)

Phantom	V_s CIRS (m/s)	Depth (mm)	V_s TOF (m/s)	$f(\hat{V}_s)$ (m/s)
1	1.27 ± 0.3	10 – 55	1.04 ± 0.00	0.92 ± 0.00
		25 – 65	1.09 ± 0.01	1.08 ± 0.00
2	2.92 ± 0.2	10 – 55	3.04 ± 0.06	2.48 ± 0.00
		25 – 65	2.76 ± 0.05	2.51 ± 0.02
3	4.02 ± 0.1	10 – 55	5.27 ± 0.14	3.68 ± 0.00
		25 – 65	4.14 ± 0.07	3.74 ± 0.01

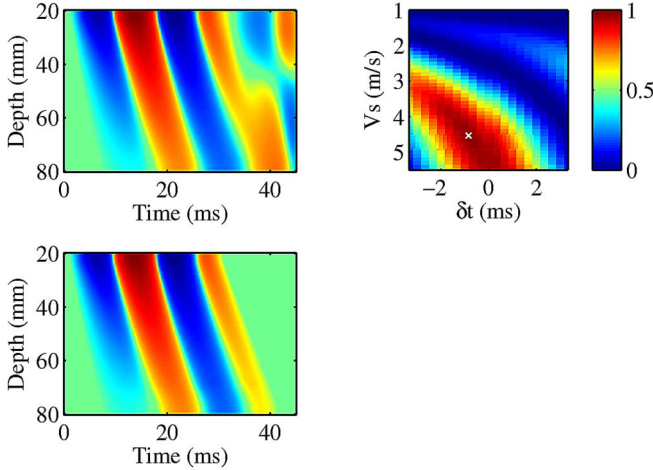


Fig. 6. ML estimation of V_s on a FEM SWPM from a $G^{\infty/2}$ geometry with $V_s = 5$ m/s, $f_a = 50$ Hz and $R = 4.5$ mm. (upper left) SWPM of the FEM-based u_s^f generated with $V_s = 5$ m/s. (upper right) ML criterion map from (7) leading to the estimate $\hat{V}_s = 4.53$ m/s. (lower left) SWPM of Green's-based u_s^G generated using $f(\hat{V}_s) = 4.91$ m/s. The same colormap as in Fig. 3 is used for the SWPMs.

that depend on the configuration and learned with the FEM simulation tool.

III. EXPERIMENTS

A. Validation of ML Estimates $f(\hat{V}_s)$ on FEM Simulations

To validate our proposed ML estimation framework, we first compared the shear wave speed V_s used in FEM simulations (the ground-truth value) for the G^{∞} and $G^{\infty/2}$ geometries to the value $f(\hat{V}_s)$ estimated with the ML criterion and post-correction, applied on the simulated SWPM. We computed error values and generated Bland–Altman plots on the database of the 369 FEM-simulated SWPMs used for the development of the method (cf. Section II-C1).

B. Validation of ML Estimates $f(\hat{V}_s)$ on RF Acquisitions From Physical Phantoms

We performed RF line acquisitions using the TE system on four phantoms. The phantoms were manufactured by CIRS Incorporated (Norfolk, VA, USA) who provides average V_s values along with standard deviation, from tests performed in static mode and on small samples of the manufactured objects. Three were homogeneous phantoms with different V_s values reported in Table II and the fourth was a heterogeneous phantom (CIRS, Model 049) that contains four sphere objects of 20 mm diameter, positioned at an approximate depth of 35 mm, and having different stiffness values which are reported in Fig. 8. The homogeneous phantoms each had a dimension of $18 \times 18 \times 9.5$ cm, filled with a homogeneous and isotropic gel [31]. The heterogeneous phantom (model 049) had a dimension of $18 \times 12 \times 9.5$ cm. The range of V_s values for the different objects was compatible with the elastographic measurement capabilities of the Fibroscan TE system. For these phantom acquisitions, the Fibroscan TE probe was operated at a frequency $f_0 = 3.5$ MHz, a bandwidth of 2.5–4.5 MHz and with a focus set at 35 mm. The probe was operated in a dedicated phantom mode to ensure that the force of the pre-constraint at the surface of the phantom remained smaller than 1N. The probe was mounted on a mechanical scanning system and positioned directly on the surface of the phantom, using a water-based ultrasound gel to ensure acoustic coupling.

For the homogeneous phantoms, ten series of RF lines were acquired for two different ranges of depth: 1) RF acquisition between 5 and 65 mm (analysis performed on the SWPMs at depth 10–50 mm); 2) RF acquisition between 20 and 80 mm (analysis performed on the SWPMs at depth 25–65 mm). RF lines were acquired with a PRF of 6 kHz and a duration of 80 ms. The probe was positioned at the center of the phantom surface.

For the heterogeneous phantom, positions of the sphere objects were not precisely known [32] and these spheres appear iso-echoic with respect to the background in B-mode images. The whole surface of the phantom was therefore scanned by translating the probe with the mechanical scanning system using a 1 mm incremental step along the x and y axis of the surface, as illustrated in Fig. 8. At each position a series of RF acquisitions was made between 15 and 55 mm in depth, with a PRF of 6 kHz and a duration of 80 ms.

C. Green's and FEM Versus RF SWPMs on Homogeneous Phantoms

Using the ML estimates ($f(\hat{V}_s), \delta t$) obtained on the three homogeneous phantoms, we generated analytical SWPMs using (3) to verify the agreement between the Green's predictions and the Fibroscan TE measures of displacements using TOF.

We also generated FEM-simulated SWPMs using the 3-D geometry of the CIRS homogeneous phantoms. Because of the cubical shape of the phantoms, we had to run the simulations on 3-D regions, without relying on axial-symmetry. We used a freely deforming top surface but fixed rigid bottom and side border conditions to replicate the phantom properties and TE recording conditions. We ran two sets of simulations, using the CIRS V_s values and the ML $f(\hat{V}_s)$ values.

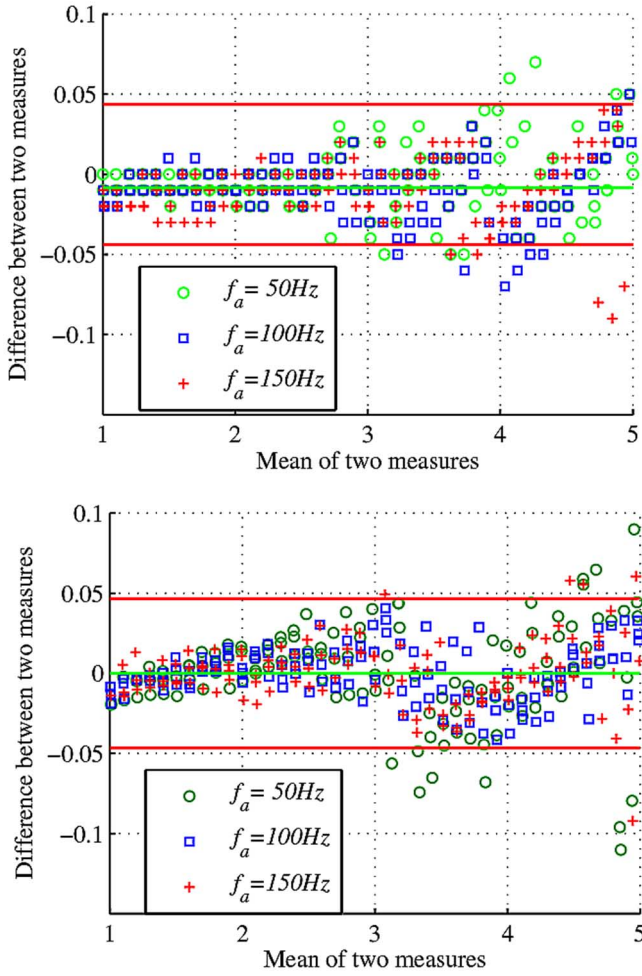


Fig. 7. Bland–Altman plots of $f(\hat{V}_s)$ versus V_s from FEM simulations on two different geometries: (top) G^∞ , (bottom) $G^{\infty/2}$.

IV. RESULTS AND DISCUSSION

Regarding the computation times, generation of the SWPM from a series of 482 RF lines acquired over 80 ms with a PRF of 6 kHz requires ~ 2 s. Estimation of V_s requires 0.05 s (for a precision of 0.03 m/s) using the TOF technique, and 3.5 s (resp. 5 s) for a precision of 0.03 (resp. 0.01) m/s using the ML estimator on a coarse (resp. fine) grid for maximization of the ML criterion.

A. Validation of ML Estimates $f(\hat{V}_s)$ on FEM Simulations

We report on the comparison of $f(\hat{V}_s)$ estimates versus ground-truth V_s values on the 369 FEM simulations with the G^∞ or $G^{\infty/2}$ geometries using a Bland–Altman analysis in Fig. 7. These plots reveal that errors are equally distributed above and below zero and that there is a slight bias leading to larger errors for larger V_s values. In the $G^{\infty/2}$ geometry, as used by the TE system, the configuration with $f_a = 50$ Hz seems to generate more outliers (i.e., larger errors).

The absolute errors have the following mean (μ_e) and standard deviation (σ_e) values.

- G^∞ : $\mu_e^\infty = 0.0171$ m/s and $\sigma_e^\infty = 0.01$ m/s.
- $G^{\infty/2}$: $\mu_e^{\infty/2} = 0.0168$ m/s and $\sigma_e^{\infty/2} = 0.01$ m/s.

B. Validation of ML Estimates $f(\hat{V}_s)$ on RF Acquisitions From Physical Phantoms

1) *Results on the Homogeneous Phantoms:* Three values of the shear wave speed of the three homogeneous phantoms, reported in Table II, are compared: the average measures provided by the CIRS manufacturer (along with their standard deviation), the values $f(\hat{V}_s)$ estimated with our ML estimator, and the values obtained with the Fibrosan TE system using the TOF commercial algorithm (for the last two measures, average and standard deviations are reported from measures made on the 10 series of RF acquisitions). Estimations with the Fibrosan TE system and the ML estimator were repeated at two different depth ranges.

We can observe that the TOF shear wave speed values are more variable over a series of measures (higher standard deviations) and vary more with respect to depth range selection than the ML estimates, especially for higher shear wave speed values. Overall, the experimental values are all in good agreements with CIRS reference values and the ML estimator systematically returned smaller V_s values. It is important to note that the V_s value provided by the CIRS manufacturer is not a physical ground-truth since it is based on an interpolation chart that CIRS learned internally from a limited set of experiments. Several recent publications have observed discrepancies of measures similar to ours using various methods of measurement. For example in [33] the V_s values corresponding to the reported Young Modulus values (E) (using the equality $E = 3\rho V_s^2$) for two CIRS phantoms with $V_s = 4.5$ (resp. 2.9) m/s had a discrepancy with respect to the tested 1-D TE system of 3.5 (resp. 0.11) m/s. In comparison, for our CIRS phantoms with $V_s = 4.02$ (resp. 2.92) m/s we have a maximal discrepancy of 0.28 (resp. 0.44) m/s with our ML method and 1.25 (resp. 0.12) m/s with the Fibrosan TOF method. Therefore the discrepancies in our measures are in agreement with the ones reported in [33]. Overall, some inherent heterogeneity in the measures of V_s can be expected due to the variable resolution of the RF signal along depth and due to the nonperfect homogeneity of the phantom.

2) *Results on the Heterogeneous Phantom:* In a heterogeneous medium, shear wave speed must be estimated locally and a TE system using TOF cannot be used to measure V_s in such condition. Regarding the ML approach, we adapted the computational framework to return a 2-D parametric image of localized V_s values as follows: ML estimations were run for each series of RF lines acquired at a given position along the x and y axis of the phantom surface (cf. Fig. 8). Instead of using the whole SWPM, ML estimations were run inside 1-D overlapping and sliding depth intervals. The length of these intervals was set empirically to 20 mm which corresponds to the smallest size returning accurate estimates, with an overlap of 99% (i.e., sliding the intervals by 0.2 mm).

This experimental and computational setup generated a parametric map of $f(\hat{V}_s)$ values within the phantom object, displayed in Fig. 8, with a spatial precision of 1 mm in x and y and 0.2 mm in depth z . We can detect three of the four spheres in the parametric map. The sphere with V_s close to the background value is not easily discernible because of the small difference between the inside and outside V_s values. Four spherical regions were manually defined so as to optimize the homo-

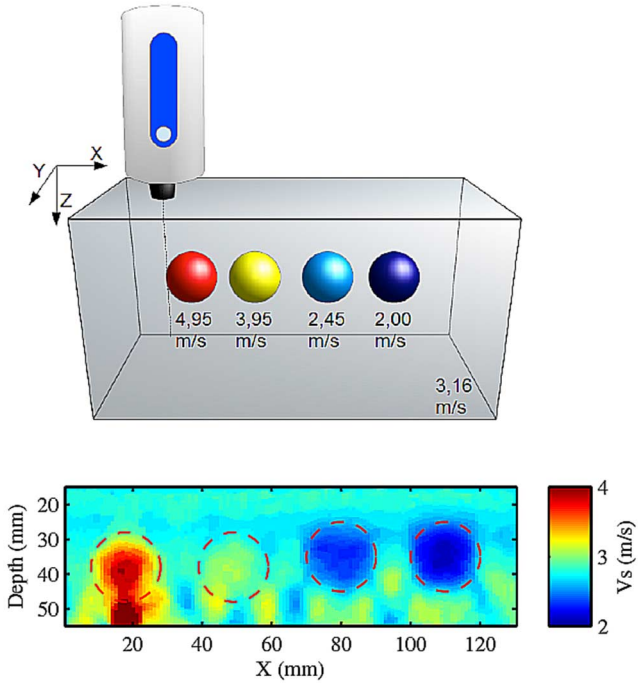


Fig. 8. Heterogeneous CIRS phantom with four spheres. (top) Schematic showing the sphere objects and the probe positioning. Average V_s values (± 0.2 m/s) provided by CIRS are reported below each sphere and in the background. (bottom) Parametric map of the ML shear wave speed estimates $f(\hat{V}_s)$. The red dashed circles represent the estimated position of the four spheres.

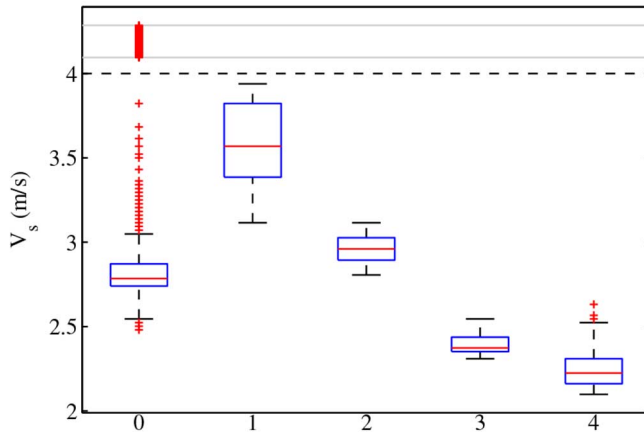


Fig. 9. Boxplots of ML estimates $f(\hat{V}_s)$ for the heterogeneous CIRS phantom, inside the background (label 0) and inside each spherical object (labels 1,2,3,4), identified on the parametric map of $f(\hat{V}_s)$.

generosity of $f(\hat{V}_s)$ inside each of them. The contours of the four regions are displayed as red dash circles in Fig. 8 on the slice along y that includes the centers of the four spheres. Boxplots of the ML estimates $f(\hat{V}_s)$ in the background (label 0) and inside the four spheres (labels 1–4) are provided in Fig. 9, with median values, 25th and 75th percentiles, whiskers on bounding values of nonoutliers, and outliers values. We can see that the background returned a rather large range of $f(\hat{V}_s)$ values while each individual sphere returned rather homogeneous ML estimates.

We further compared our estimates to the values reported by three studies which used the same CIRS phantom model:

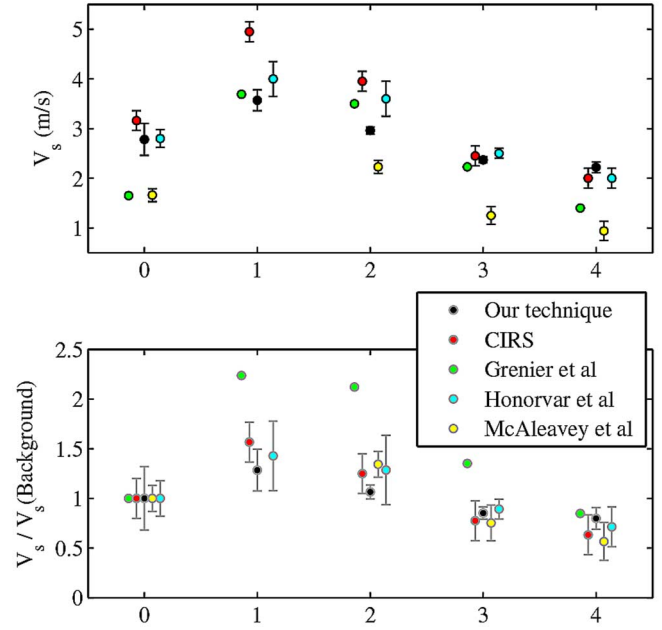


Fig. 10. Mean and standard deviation of $f(\hat{V}_s)$ for the CIRS heterogeneous phantom, compared to values reported in three papers and by the manufacturer. Labels correspond to: the background (0) and inside each spherical object (1,2,3,4), identified on the parametric map of $f(\hat{V}_s)$. Absolute (top) and relative (bottom) values are reported, after normalization with respect to the background V_s measure.

the study in [32] which used magnetic resonance elastography (MRE) and the studies in [34], [35] which used ultrasound elastography (US-E). Results of this comparison, summarized in Fig. 10, confirm that shear wave speed estimates agree rather well between studies and could differ quite significantly from the values provided by the manufacturer. We cannot expect perfect agreement between the estimated V_s values since the precise position of the spheres is unknown, phantom objects are all slightly different and measurement techniques are all imperfect: for example MRE V_s parametric maps are usually less noisy than US-E maps but have a lower spatial resolution.

C. Green's and FEM Versus RF SWPMS on Homogeneous Phantoms

We illustrate in Fig. 11 the visual correspondence achieved for the homogeneous phantoms between the SWPMS from the Fibrosan TE recordings and the Green's analytical predictions using the ML estimates $f(\hat{V}_s)$ and $\hat{\delta}t$. The SWPMS recorded with the Fibrosan TE system show two types of artefacts: a deformation of the wave near the surface, due to coupling of compression and shear waves, and rebounds generated at the bottom of the phantom objects. We clearly observe that, as the elasticity of the medium increases (i.e., as V_s increases), the amplitude and the spatial extent of the rebounds increase, leading to potentially inaccurate estimations of V_s using the TOF graphical method. The analytical SWPMS look remarkably similar to the Fibrosan TE recordings, replicating correctly the extent of the coupling zone (which increases with V_s) as well as the attenuation of the shear wave intensity in depth. The main difference is the absence of rebounds. Indeed, rebounded waves are not

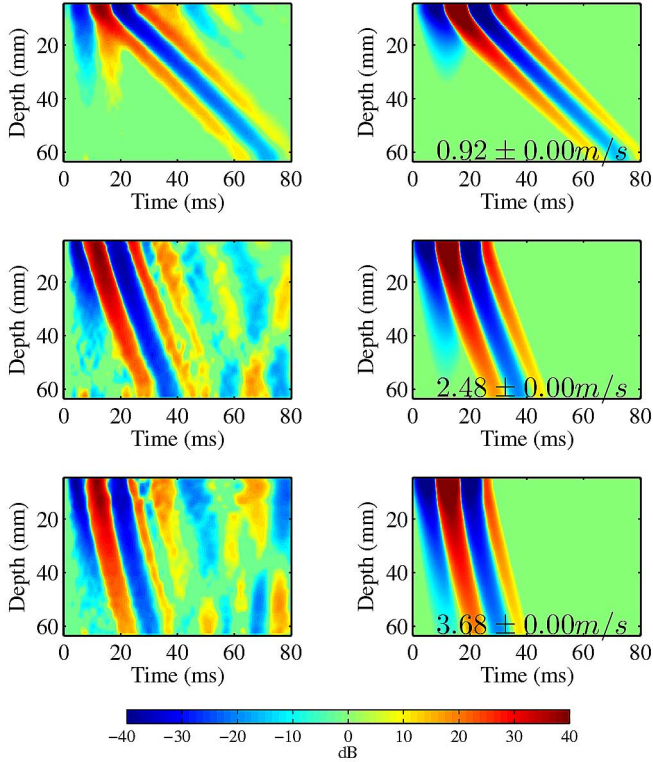


Fig. 11. SWPMs of displacements from Green's estimates and the recordings from the Fibrosan TE system for the three homogeneous CIRS phantoms (one per line) with CIRS $V_s = 1.27, 2.92, 4.02$ m/s. For each line: (left column) Fibrosan TE recordings and (right column) analytical Green's-based SWPMs using the ML estimates $f(\hat{V}_s)$ and δt . Average values of $f(\hat{V}_s)$ are reported for each phantom.

found on the synthetical SWPMs since the medium is assumed infinite.

The ML computational pipeline, with its corrected Green's model, is therefore overall in good agreement with the observations from the Fibrosan TE system for homogeneous mediums.

In addition, we report in Fig. 12 the FEM-simulated SWPMs for the three homogeneous phantoms using the CIRS V_s values and the ML $f(\hat{V}_s)$ values. Comparing the Fibrosan TE recordings and the 3-D FEM simulations, we see that the FEM simulations are able to replicate quite fairly the presence or absence of rebounds as well as the general shape (including the coupling zone) and slope of the shear wave propagating in the homogeneous medium. Results on the top line (with the lowest V_s value) clearly show that the provided CIRS V_s value is less accurate than our ML estimation for the simulation of the Fibrosan recordings. Detailed numerical comparisons of these SWPMs is left for future work.

Regarding the systematic offset δt (1–5 ms) observed on the temporal onsets of the displacements u_3^G when compared to u_3^F and post-corrected with the estimated δt , this phenomenon was previously reported for the semi-infinite geometry on phantom-based experiments in Sandrin *et al.* [11], but no specific explanation was provided. Given that the value of this offset depends on the experimental setup, we can make the hypothesis that it could be due to the simplistic baffled conditions used to derive the Green's functions that do not represent well the influence of the interface membrane on the waves that are actually transmitted in the FEM and *in vitro* experiments. An experimental

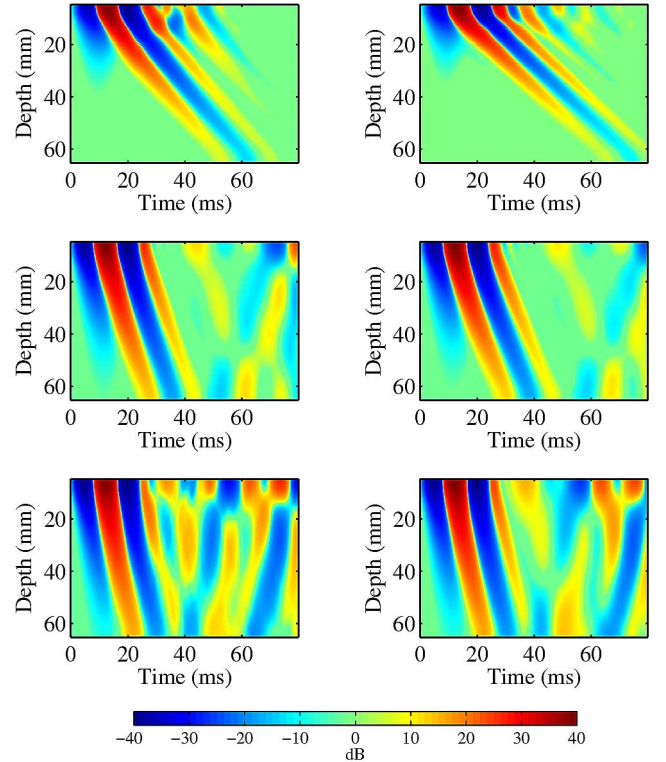


Fig. 12. FEM-simulated SWPMs of displacements for the three homogeneous CIRS phantoms (one per line) using: (left) the CIRS values $V_s = 1.27, 2.92, 4.02$ m/s and (right) the ML estimated values $f(\hat{V}_s) = 0.92, 2.48, 3.68$ m/s.

setup using a truly baffled piston could be implemented to test this hypothesis.

V. CONCLUSION

We introduced in this work a novel ML framework for the estimation of the shear wave speed on 1-D RF lines acquired with the transient elastography framework used by TE systems.

The proposed ML estimator exploits an analytical approximation of the displacements induced in the medium provided by the Green's functions previously derived for the geometry of a semi-infinite medium hit by a circular piston. Our methodological developments exploit a numerical simulation toolbox, using FEM. This toolbox was previously validated to accurately simulate TE acquisitions, and was used in this work to analyze the capacity of the Green's functions to match TE displacement measures. Our developments reveal that the Green's approximations can be exploited to analyze displacements simulated or recorded on real RF lines, at the condition of introducing auxiliary variables in the ML formulation to account for temporal delays and depth-dependent attenuation. These auxiliary variables are jointly estimated, along with the shear wave speed V_s , via the maximization of an original ML criterion.

Finally, a correction of the ML estimate of V_s in semi-infinite mediums is required, which we formulate as a quadratic function whose coefficients depend on the stress configuration.

Our method was validated on FEM simulations and TE acquisitions made on three homogeneous phantoms with different elasticities and on a heterogenous phantom. In all cases, estimated shear wave speed values were close to the ground-truth

values. The reported errors and variability of the measures are in agreement with results found in the literature.

Overall, the proposed ML estimation framework enables the following improvements over the current TOF algorithm used by most TE systems to estimate the shear wave speed V_s : 1) ability to compute localized estimates of V_s in heterogeneous mediums; 2) estimations of shear wave speeds that are invariant with respect to the depth of the acquisitions; 3) robustness of the shear wave speed estimates to physical effects such as wave rebounds; 4) ability to compute shear wave speed estimates in high elasticity mediums (i.e., with $V_s > 5$ m/s) that the TOF technique cannot handle robustly; 5) ability to compute shear wave speed on thin layers.

APPENDIX DERIVATION OF THE ML CRITERION

The ML function to minimize in (6) is written as

$$L(\beta, V_s, \delta t) = \sum_{m=1}^M \sum_{n=1}^N (y[m, n] - \beta[m] u_3[m, n; V_s; \delta t])^2. \quad (9)$$

We first obtain the ML value $\hat{\beta}$ of β analytically, by setting to 0 the derivative $\partial L(\beta, V_s, \delta t)/\partial \beta$

$$\begin{aligned} \frac{\partial L(\beta, V_s, \delta t)}{\partial \beta} &= -2 \sum_{m=1}^M \sum_{n=1}^N (y[m, n] - \beta[m] u_3[m, n; V_s; \delta t]) \\ &\times u_3[m, n; V_s; \delta t] = 0 \end{aligned} \quad (10)$$

$$\forall m, \hat{\beta}[m] = \frac{\sum_{n=1}^N y[m, n] u_3[m, n; V_s; \delta t]}{\sum_{n=1}^N u_3^2[m, n; V_s; \delta t]}. \quad (11)$$

Then, inserting $\hat{\beta}$ in the function $L(\beta, V_s, \delta t)$ we get

$$\begin{aligned} L(\hat{\beta}, V_s, \delta t) &= \sum_{m=1}^M \sum_{n=1}^N |y[m, n] - \hat{\beta}[m] u_3[m, n; V_s; \delta t]|^2 \\ &= \sum_{m=1}^M \sum_{n=1}^N y[m, n] (y[m, n] - \hat{\beta}[m] u_3[m, n; V_s; \delta t]) \\ &\quad - \underbrace{\sum_{m=1}^M \hat{\beta}[m] \sum_{n=1}^N (u_3[m, n; V_s; \delta t] (y[m, n] - \hat{\beta}[m] u_3[m, n; V_s; \delta t]))}_{=0 \text{ from 11}} \\ &= \sum_{m=1}^M \sum_{n=1}^N y^2[m, n] - \sum_{m=1}^M \hat{\beta}[m] \sum_{n=1}^N y[m, n] u_3[m, n; V_s; \delta t] \\ &= \sum_{m=1}^M \sum_{n=1}^N y^2[m, n] - \sum_{m=1}^M \frac{(\sum_{n=1}^N y[m, n] u_3[m, n; V_s; \delta t])^2}{\sum_{n=1}^N u_3^2[m, n; V_s; \delta t]}. \end{aligned} \quad (12)$$

Since the first term does not depend on the parameters $(V_s, \delta t)$, minimizing the function $L(\hat{\beta}, V_s, \delta t)$ is equivalent to maximizing the second term on the right in (12), which is positive. We end up with the following maximization criterion:

$$\begin{aligned} (\hat{V}_s, \hat{\delta t}) &= \operatorname{argmin}_{V_s, \delta t} L(\hat{\beta}, V_s, \delta t) \\ &= \operatorname{argmax}_{V_s, \delta t} \sum_{m=1}^M \frac{\left(\sum_{n=1}^N y[m, n] u_3[m, n; V_s; \delta t] \right)^2}{\sum_{n=1}^N u_3^2[m, n; V_s; \delta t]} \end{aligned} \quad (13)$$

leading to the ML function and criterion of (7). We point out that the criterion in (13) can be modified by multiplying the denominator by terms in $y[m, n]$ without changing the maximization problem, which leads to rewriting it as the maximization of the correlation between $y[m, n]$ and $u_3[m, n; V_s; \delta t]$

$$\begin{aligned} (\hat{V}_s, \hat{\delta t}) &= \operatorname{argmax}_{V_s, \delta t} \sum_{m=1}^M \frac{\left(\sum_{n=1}^N y[m, n] u_3[m, n; V_s; \delta t] \right)^2}{\left(\sum_{n=1}^N u_3^2[m, n; V_s; \delta t] \right) \left(\sum_{n=1}^N y^2[m, n] \right)}. \end{aligned} \quad (14)$$

ACKNOWLEDGMENT

The authors would like to thank the INSERM research unit U930 for lending their CIRS phantom model 049.

REFERENCES

- [1] L. Sandrin, B. Fourquet, J. M. Hasquenoph, S. Yon, C. Fournier, F. Mal, C. Christidis, M. Ziou, B. Poulet, F. Kazemi, M. Beaugrand, and R. Palau, "Transient elastography: A new noninvasive method for assessment of hepatic fibrosis," *Ultrasound Med. Biol.*, vol. 29, no. 12, pp. 1705–1713, 2003.
- [2] M. Fatemi and J. F. Greenleaf, "Vibro-acoustography: An imaging modality based on ultrasound-stimulated acoustic emission," *Proc. Nat. Acad. Sci. USA*, vol. 96, no. 12, pp. 6603–6608, 1999.
- [3] E. Konofagou and K. Hynynen, "Harmonic motion imaging: A new technique for the estimation of mechanical properties in tissues," *Ultrasound Med. Biol.*, vol. 29, no. 5, pp. S59–S59, 2003, Suppl. 1.
- [4] J. Bercoff, M. Tanter, and M. Fink, "Supersonic shear imaging: A new technique for soft tissue elasticity mapping," *IEEE Trans. Ultrason., Ferroelectr. Freq. Control*, vol. 51, no. 4, pp. 396–409, Apr. 2004.
- [5] K. R. Nightingale, M. L. Palmeri, R. W. Nightingale, and G. E. Trahey, "On the feasibility of remote palpation using acoustic radiation force," *J. Acoust. Soc. Am.*, vol. 110, no. 1, pp. 625–634, 2001.
- [6] E. Bavu, J. L. Gennisson, M. Couade, J. Bercoff, V. Mallet, M. Fink, A. Badel, A. Vallet-Pichard, B. Nalpas, M. Tanter, and S. Pol, "Noninvasive in vivo liver fibrosis evaluation using supersonic shear imaging: A clinical study on 113 hepatitis c virus patients," *Ultrasound Med. Biol.*, vol. 37, no. 9, pp. 1361–1373, 2011.
- [7] S. A. Kruse, G. H. Rose, K. J. Glaser, A. Manduca, J. P. Felmlee, C. R. Jack, Jr, and R. L. Ehman, "Magnetic resonance elastography of the brain," *NeuroImage*, vol. 39, no. 1, pp. 231–237, 2008.
- [8] D. Cosgrove, F. Piscaglia, J. Bamber, J. Bojunga, J. M. Correas, O. H. Gilja, A. S. Klausner, I. Sporea, F. Calliada, V. Cantisani, M. D'Onofrio, E. E. Drakonaki, M. Fink, M. Friedrich-Rust, J. Fromageau, R. F. Havre, C. Jenssen, R. Ohlinger, A. Saftoiu, F. Schaefer, and C. F. Dietrich, "EFSUMB guidelines and recommendations on the clinical use of ultrasound elastography. Part 2: Clinical applications," *Ultraschall in der Medizin (Stuttgart, Germany: 1980)*, vol. 5, no. 10, pp. 1214–1220, 2013.

- [9] L. Castera, J. Vergniol, J. Foucher, B. Le Bail, E. Chanteloup, M. Haaser, M. Darriet, P. Couzigou, and V. De Ledinghen, "Prospective comparison of transient elastography, fibrotest, APRI, and liver biopsy for the assessment of fibrosis in chronic hepatitis C," *Gastroenterology*, vol. 128, no. 2, pp. 343–350, 2005.
- [10] M. Friedrich-Rust, M. F. Ong, E. Herrmann, V. Dries, P. Samaras, S. Zeuzem, and C. Sarrazin, "Real-time elastography for noninvasive assessment of liver fibrosis in chronic viral hepatitis," *Am. J. Roentgenology*, vol. 188, no. 3, pp. 758–64, 2007.
- [11] L. Sandrin, M. Tanter, J. L. Gennisson, S. Catheline, and M. Fink, "Shear elasticity probe for soft tissues with 1-D transient elastography," *IEEE Trans. Ultrason., Ferroelectr. Freq. Control*, vol. 49, no. 4, pp. 436–446, Apr. 2002.
- [12] J. A. Talwalkar, D. M. Kurtz, S. J. Schoenleber, C. P. West, and V. M. Montori, "Ultrasound-based transient elastography for the detection of hepatic fibrosis: Systematic review and meta-analysis," *Clin. Gastroenterol. Hepatol.*, vol. 5, no. 10, pp. 1214–1220, 2007.
- [13] T. E. Oliphant, A. Manduca, R. L. Ehman, and J. F. Greenleaf, "Complex-valued stiffness reconstruction for magnetic resonance elastography by algebraic inversion of the differential equation," *Magn. Reson. Med.*, vol. 45, no. 2, pp. 299–310, 2001.
- [14] A. Manduca, T. E. Oliphant, M. A. Dresner, J. L. Mahowald, S. A. Kruse, E. Amromin, J. P. Felmlee, J. F. Greenleaf, and R. L. Ehman, "Magnetic resonance elastography: Non-invasive mapping of tissue elasticity," *Med. Image Anal.*, vol. 5, no. 4, pp. 237–254, 2001.
- [15] M. L. Palmeri, M. H. Wang, J. J. Dahl, K. D. Frinkley, and K. R. Nightingale, "Quantifying hepatic shear modulus in vivo using acoustic radiation force," *Ultrasound Med. Biol.*, vol. 34, no. 4, pp. 546–558, 2008.
- [16] M. L. Palmeri, A. C. Sharma, R. R. Bouchard, R. W. Nightingale, and K. R. Nightingale, "A finite-element method model of soft tissue response to impulsive acoustic radiation force," *IEEE Trans. Ultrason., Ferroelectr., Freq. Control*, vol. 52, no. 10, pp. 1699–1712, Oct. 2005.
- [17] Q. Chen, S. I. Ringleb, A. Manduca, R. L. Ehman, and K.-N. An, "A finite element model for analyzing shear wave propagation observed in magnetic resonance elastography," *J. Biomechan.*, vol. 38, no. 11, pp. 2198–2203, 2005.
- [18] C. Bastard, J. P. Remenieras, S. Calle, and L. Sandrin, "Simulation of shear wave propagation in a soft medium using a pseudospectral time domain method," *J. Acoust. Soc. Am.*, vol. 126, no. 4, pp. 2108–2116, 2009.
- [19] L. Sandrin, D. Cassereau, and M. Fink, "The role of the coupling term in transient elastography," *J. Acoust. Soc. Am.*, vol. 115, no. 1, pp. 73–83, 2004.
- [20] S. Audière, M. Charbit, E. Angelini, J. Oudry, and L. Sandrin, "Finite element simulation of shear wave propagation induced by a VCTE probe," in *COMSOL Conf.*, Oct. 2010.
- [21] M. Charbit, E. Angelini, and S. Audière, "Maximum likelihood estimation of Young's modulus in transient elastography with unknown line-of-sight orientation," in *Proc. 9th IEEE Int. Symp. Biomed. Imag.*, 2012, pp. 1108–1111.
- [22] A. Lhemery, "A model for the transient ultrasonic field radiated by an arbitrary loading in a solid," *J. Acoust. Soc. Am.*, vol. 96, no. 6, pp. 3776–3786, 1994.
- [23] A. E. H. Love, *The Mathematical Theory of Elasticity*. New York: Dover, 1944.
- [24] J. D. Achenbach, "Applied mathematics and mechanics," in *Wave Propagation in Elastic Solids*. Amsterdam, The Netherlands: North-Holland, 1990.
- [25] K. Aki and P. G. Richards, *Quantitative Seismology: Theory and Methods*, 2nd ed. Herndon, VA: University Sci. books, 2002.
- [26] R. Sinkus, M. Tanter, T. Xydeas, S. Catheline, J. Bercoff, and M. Fink, "Viscoelastic shear properties of in vivo breast lesions measured by MR elastography," *Magn. Reson. Imag.*, vol. 23, no. 2, pp. 159–165, 2005.
- [27] S. Roth, J. Oudry, M. El Rich, and H. Shakourzadeh, "Influence of mesh density on a finite element models response under dynamic loading," *J. Biol. Phys. Chem.*, vol. 9, no. 4, pp. 203–209, 2009.
- [28] G. R. Harris, "Review of transient field theory for a baffled planar piston," *J. Acoust. Soc. Am.*, vol. 70, no. 1, pp. 10–20, 1981.
- [29] J. A. Jensen and N. B. Svendsen, "Calculation of pressure fields from arbitrarily shaped, apodized, and excited ultrasound transducers," *IEEE Trans. Ultrason., Ferroelectr. Freq. Control*, vol. 39, no. 2, pp. 262–267, Mar. 1992.
- [30] G. Frisk, *Ocean and Seabed Acoustics: A Theory of Wave Propagation*. Upper Saddle River, NJ: Prentice-Hall, 1994.
- [31] R. Q. Erkamp, P. Wiggins, A. R. Skovoroda, S. Y. Emelianov, and M. O'Donnell, "Measuring the elastic modulus of small tissue samples," *Ultrasound Imag.*, vol. 20, no. 1, pp. 17–28, 1998.
- [32] M. Honarvar, R. S. Sahebjavaher, S. E. Salcudean, and R. Rohling, "Sparsity regularization in dynamic elastography," *Phys. Med. Biol.*, vol. 57, no. 19, p. 5909, 2012.
- [33] H. Xie, V. Shandasani, Z. Heng, S. Pengfei, Z. Shiwei, J.-L. Robert, J. Greenleaf, and C. Shigao, "A phantom study to cross-validate multi-modality shear wave elastography techniques," in *Proc. IEEE Int. Ultrason. Symp.*, 2012, pp. 1858–1861.
- [34] S. McAleavey, M. Menon, and E. Eleggbe, "Shear modulus imaging with spatially-modulated ultrasound radiation force," *Ultrason. Imag.*, vol. 31, no. 4, pp. 217–234, 2009.
- [35] D. Grenier, E. Brusseau, H. Liebgott, F. Duboeuf, F. Pilleul, and O. Beuf, "MR-elastography versus quasi-static US-elastography," *ESMRMB*, p. 366, 2009.